

External control of electron energy distributions in a dual tandem inductively coupled plasma

Lei Liu,¹ Shyam Sridhar,¹ Weiye Zhu,^{1,a)} Vincent M. Donnelly,^{1,b)} Demetre J. Economou,^{1,c)} Michael D. Logue,² and Mark J. Kushner^{2,d)}

¹Plasma Processing Laboratory, Department of Chemical and Biomolecular Engineering, University of Houston, Houston, Texas 77204-4004, USA

²Department of Electrical Engineering and Computer Science, University of Michigan, Ann Arbor, Michigan 48109-2122, USA

(Received 12 June 2015; accepted 17 July 2015; published online 27 August 2015)

The control of electron energy probability functions (EPPFs) in low pressure partially ionized plasmas is typically accomplished through the format of the applied power. For example, through the use of pulse power, the EEPF can be modulated to produce shapes not possible under continuous wave excitation. This technique uses *internal control*. In this paper, we discuss a method for *external control* of EEPFs by transport of electrons between separately powered inductively coupled plasmas (ICPs). The reactor incorporates dual ICP sources (main and auxiliary) in a tandem geometry whose plasma volumes are separated by a grid. The auxiliary ICP is continuously powered while the main ICP is pulsed. Langmuir probe measurements of the EEPFs during the afterglow of the main ICP suggests that transport of hot electrons from the auxiliary plasma provided what is effectively an external source of energetic electrons. The tail of the EEPF and bulk electron temperature were then elevated in the afterglow of the main ICP by this *external* source of power. Results from a computer simulation for the evolution of the EEPFs concur with measured trends. © 2015 AIP Publishing LLC. [<http://dx.doi.org/10.1063/1.4928870>]

I. INTRODUCTION

The electron energy probability function (EPPF) (or its normalized electron energy distribution, EED) in low temperature plasmas employed for microelectronics fabrication is critical to control the fluxes of radicals and ions striking the substrate.^{1,2} As feature sizes continue to shrink to the sub-15 nm regime, tailoring the shape of the EEPF becomes increasingly important to selectively control the fragmentation of feedstock gases by electron impact collisions.³ Many methods have been employed to control or manipulate the EEPF or electron temperature (T_e).⁴ Some of these methods include varying the plasma operating space (e.g., frequency, power),⁵ pulsed plasma excitation,^{6–8} and the use of an external applied axial magnetic field to control T_e in an inductively coupled plasma (ICP).⁹ These methods may be considered *internal control* since the plasma for which the EEPF is being controlled is being directly acted upon. *External control* of EEPFs includes methods of control not directly applied to the plasma of interest and so involves transport of species from one site to another. One such *external control* method for manipulating T_e is the use of a biased grid separating a plasma region from the ensuing downstream region,^{10,11} a configuration investigated by Hong *et al.*¹² Magnetic filters, discussed by Aanesland *et al.*,¹³ selectively pass a portion of the EEPF and can be considered an external control method. Uhm *et al.*¹⁴ used a

dual ICP system consisting of a remote ICP co-axial with a main ICP, with no grid separating the two plasmas. By adjusting the value of a series variable capacitor at the end of the main ICP coil, they could vary the plasma density and T_e .

In this paper, we discuss an *external control* method to manipulate the EEPF in a pulsed, low pressure ICP. The reactor consists of two ICP sources in a tandem geometry separated by a grid. One of the ICPs is operated in a continuous mode, while the second is operated in a pulsed mode. Langmuir probe measurements and computer modeling were performed for the tandem ICP system. We found that during the afterglow of the pulsed plasma, the EEPF and so T_e could be controlled by hot electron transport from the continuously operated ICP.

II. DESCRIPTION OF THE EXPERIMENT AND MODEL

The experimental apparatus, consisting of two co-axial (tandem) ICPs, is shown in Fig. 1. The main ICP (lower plasma) was sustained in a 17.8 cm long, 8.6 cm inside diameter water-cooled alumina tube.^{15,16} The gas is argon at pressures of ≈ 14 – 16 mTorr. The auxiliary ICP (upper plasma) was sustained in a 33.0 cm long, 7.9 cm inside diameter water-cooled alumina tube. Faraday shields on the outside cylindrical surfaces of the alumina tubes of both ICPs minimized capacitive coupling between the coils and the plasmas. The Faraday shields were electrically grounded. The 13.56 MHz power supplied to the main plasma in which the EEPFs were investigated was pulsed at 10 kHz (100 μ s pulsed period), with a duty cycle of 20% (20 μ s power on, 80 μ s power off). The nominal time-averaged power to the

^{a)}Present Address: Lam Research Corp., 4650 Cushing Parkway, Fremont, California 94538, USA.

^{b)}vmdonnelly@uh.edu

^{c)}economou@uh.edu

^{d)}mjkush@umich.edu

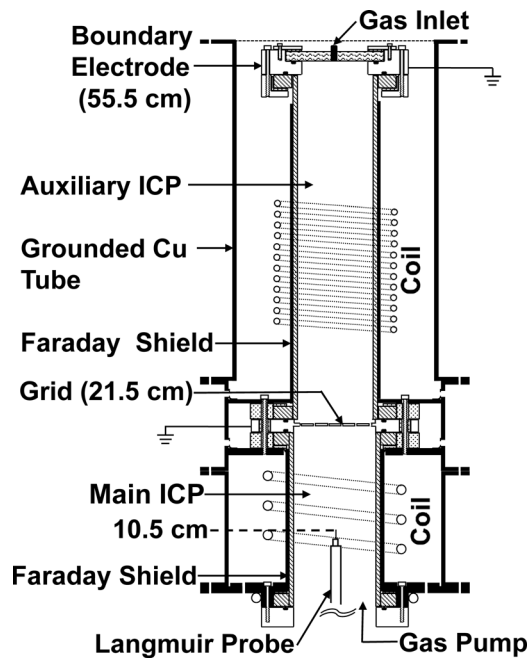


FIG. 1. Schematic of the experimental apparatus with dual tandem inductively coupled plasma (ICP) sources. The auxiliary (upper) ICP is separated from the main (lower) ICP by a grid.

main plasma was 100 W. The auxiliary plasma was operated in a continuous wave (cw) mode with nominal power of 500 W at 13.26 MHz. The 300 kHz difference in frequency between the two sources is large enough so that noise in the electronics, including the Langmuir probe signal, due to RF pickup on wires and ground loops is not a serious problem. However, the 13.26 MHz is close enough to 13.56 MHz that the RF chokes in the Langmuir probe (designed for 13.56 MHz) still provide blockage of residual small RF currents collected at the fundamental and harmonics frequencies. Nonetheless, there is some added noise to the Langmuir probe when both sources are operated due to this effect.

The reported power is that measured by directional power-meters. Given that the electron density during the late afterglow predicted by the simulation was within the experimental uncertainty, the power transfer efficiency appears to be high. The ICPs were separated by a 9.5 cm-diameter, 90% transparent, grounded tungsten grid, with 2.4 mm square openings. The sheath thickness near the grid was $\approx 200 \mu\text{m}$, which is much smaller than the holes of the grid separating the two sources. This arrangement allowed cross-talk between the two plasmas depending on their relative plasma potentials, V_p .¹⁷ In fact, experiments and simulations found little difference if this grid was removed, most likely due to the large openings and the high transparency of the grid. Its presence provided some return path for electrons withdrawn by the Langmuir probe, described below, at higher positive voltages. Ar (80 standard cm^3/min) was injected at the top of the auxiliary plasma and pumped from the bottom of the main plasma. For a measured pressure of 14 mTorr at the center of the lower plasma, the pressure in the middle of the upper plasma was estimated to be 16 mTorr.

A Langmuir probe (Scientific Systems Smartprobe) was used to measure ion and electron densities (n_i and n_e) and the

EEDF. Measurements were made along the axis of the reactor in the main plasma, 11 cm below the grid. The cylindrical tungsten probe tip had a diameter of 0.18 mm and was 6.5 mm long but the exposed length was only 1.5 mm, with the remaining 5 mm covered by a 0.51 mm outside diameter ceramic tube. The electron density and average electron energy were calculated as integrals over the measured EEDF, which was smoothed using 5-point averaging. T_e was calculated as $2/3 \langle \epsilon \rangle$, where $\langle \epsilon \rangle$ is the average electron energy. As noted above, the probe was RF compensated although RF interference is not expected to be an issue since both ICPs were Faraday shielded to block RF oscillations of the plasma potential.

The system was modeled using the Hybrid Plasma Equipment Model (HPEM).^{18–20} The HPEM combines fluid and kinetic modules that exchange information on an iterative basis. The model geometry, and computed electron number densities and ionization rates (described below) are shown in Fig. 2. The Electromagnetics Module (EMM), the Electron Energy Transport Module (EETM), and the Fluid-Kinetics Module (FKM) of the HPEM were used. The

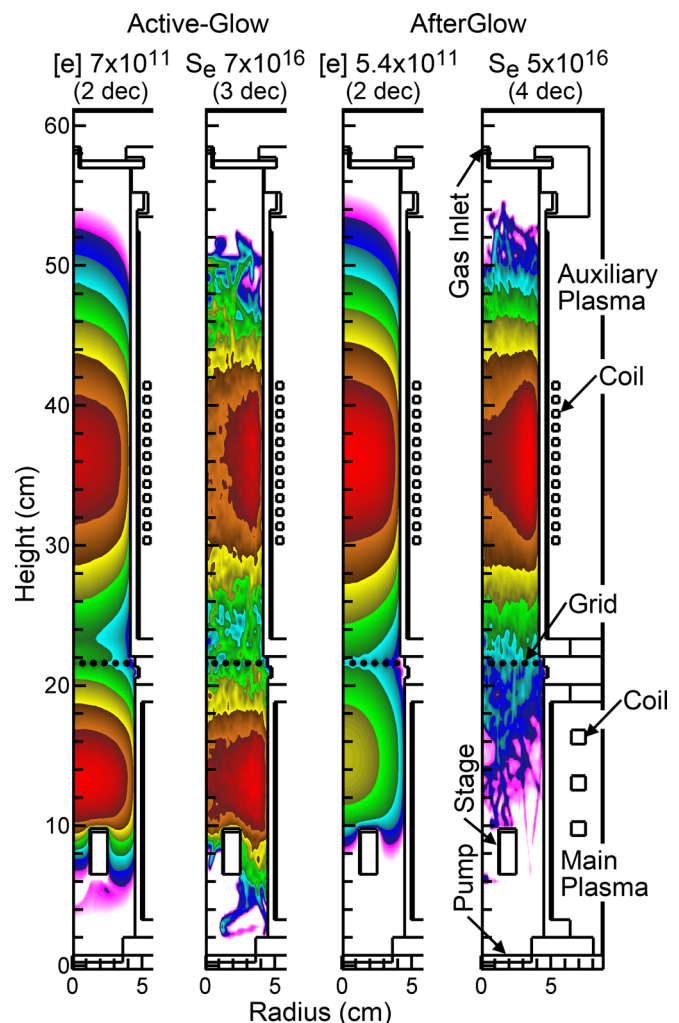


FIG. 2. Computational geometry and predicted plasma properties for electron density ($[e]$, cm^{-3}) and electron impact ionization source (S_e , $\text{cm}^{-3} \text{s}^{-1}$) for argon at ≈ 15 mTorr. Results are shown (left) at the end of the active-glow and (right) end of the afterglow. The contours are a log scale over the indicated decades with the maximum value shown in each frame.

inductively coupled electromagnetic fields were produced in the EMM by solving a frequency domain implementation of the wave equation. The spatially and time dependent EEDs or EEPFs were produced in the EETM using an electron Monte Carlo simulation (eMCS).²⁰ Electromagnetic fields for the eMCS were provided by the EMM, and electrostatic fields were provided by the FKM. The Faraday shield was accounted for by not allowing electrostatic fields from the coil to penetrate into the plasma. Electrostatic fields produced by the plasma were included. The eMCS included algorithms for electron-electron collisions and also provided kinetically derived antenna driven currents and power deposition for use in the EMM. The rate coefficients produced by the EEDs were used in the FKM where continuity, momentum, and energy equations were solved for all charged and neutral species. With gas injection at the top of the chamber and pumping at the bottom, a pressure drop of a few mTorr naturally results from solving the compressible form of the neutral transport equations. This pressure drop is commensurate with the experimental measurements.

Algorithms were developed to enable power deposition for each coil to be separately specified and for electron currents generated in the eMCS to be allocated to the coils. Power delivered by each coil to the plasma are inputs to the model. The antenna currents are then adjusted during execution of the model to deliver the specified power.

For pulsed operation, the simulation started by computing the steady-state conditions for the time-averaged power deposition after which pulsing began. The EEDs during a pulse period were resolved by 200 time slices to provide time dependent distributions. The grid between the two plasma sources was included in the model by specifying that individual computational mesh points had metal properties and were at ground potential. These boundary conditions were then used in solution of Poisson's equation for the electric potential. The spacing of the metal mesh points and effective collection areas were chosen to approximate those in the experiment. The argon reaction mechanism is essentially the same as described in Ref. 21, except that the two metastable levels (Ar[1s₅], Ar[1s₃]) are combined into a single level, and the two resonant states (Ar[1s₄], Ar[1s₂]) are combined into a single level.

III. EXTERNAL CONTROL OF EEPFs

Experimentally measured time-resolved electron temperature T_e and electron density n_e are shown in Fig. 3 for only the main (lower) plasma on and auxiliary plasma off; and with both plasmas on. The main plasma was turned on to start the active-glow at time $t \approx 0 \mu\text{s}$ and turned off (start of 80 μs of afterglow) at $t \approx 20 \mu\text{s}$. During the active-glow, T_e rapidly overshoots its steady state value and then reaches a quasi-steady state for the duration of the plasma-on period. The overshoot results from the need to avalanche the plasma density, and this phenomenon has been previously observed experimentally and predicted computationally.^{7,19} n_e increases by 3 to 4 times from the pre-pulse value, reaching $5.4 \times 10^{11} \text{ cm}^{-3}$ when only the main plasma is on and $4 \times 10^{11} \text{ cm}^{-3}$ when both plasmas are on.

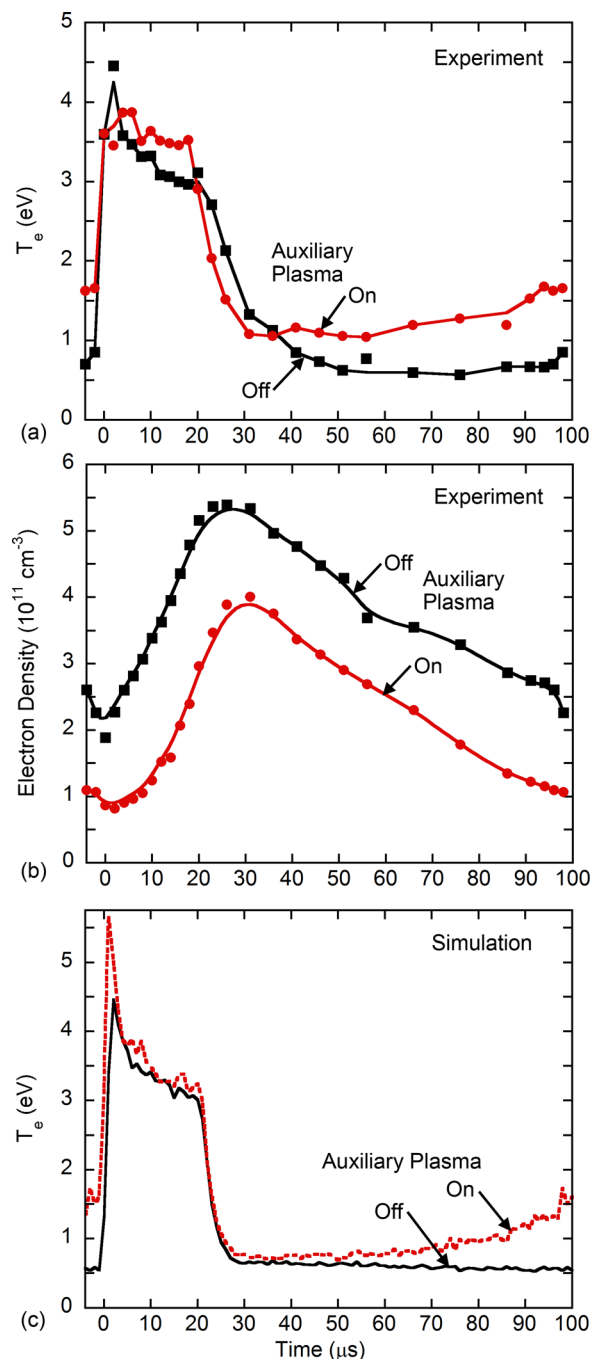


FIG. 3. Time-resolved experimentally measured (a) electron temperature (T_e) and (b) electron density for the pulsed main plasma with and without the cw auxiliary plasma for argon at ≈ 15 mTorr. (c) Predictions of the electron temperature from the model.

When only the main plasma is on, after the power is turned off (at $t \approx 20 \mu\text{s}$), T_e decreases and within 20 μs reaches an almost constant value of 0.7 eV for the remainder of the afterglow. When the upper, auxiliary cw plasma is also on, after an initial decay to 1.0 eV, T_e increases to 1.7 eV at the end of the afterglow.

Experimentally measured and computed time-resolved EEPFs are shown in Fig. 4 for only the main lower (pulsed) plasma being on. EEPFs are shown in Fig. 5 for when the auxiliary upper (cw) plasma is also on. EEPFs are shown for $t = 18 \mu\text{s}$ ($\approx 2 \mu\text{s}$ before the end of the active glow), $t = 23 \mu\text{s}$

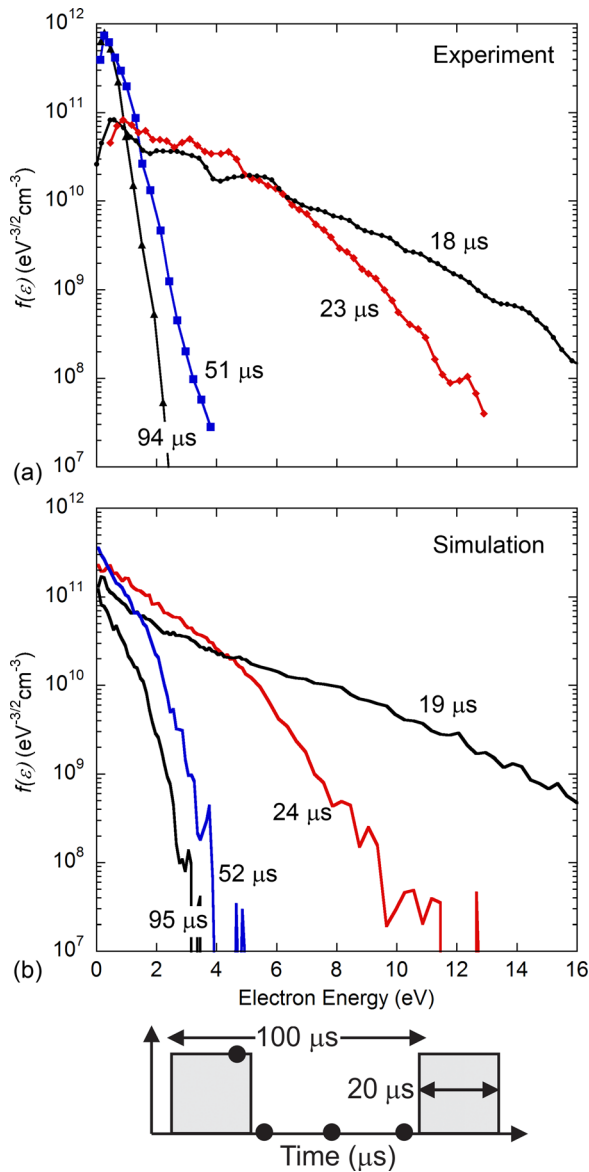


FIG. 4. Time-resolved electron energy probability functions (EPPFs) when only the pulsed main plasma is on, obtained from the (a) experiment and (b) simulation. The times of the EPPFs relative to the start of the 20 μs power pulse are shown in the lower schematic.

($\approx 3 \mu\text{s}$ into the afterglow), $t = 51 \mu\text{s}$ (in the middle of the afterglow), and $t = 94 \mu\text{s}$ (late in the afterglow).

The time-dependent behavior of T_e and the EEPF with only the main plasma on is well understood.^{22–24} T_e increases when applying power and overshoots the quasi-steady value as power is initially delivered to a smaller number of electrons. To avalanche the electron density to a higher value during the power pulse, T_e must at some point exceed the steady-state value. If the power pulse is long enough, T_e approaches the lower, quasi-steady value. The tail of the EEPF is extended to high energy, and the electron distribution is fairly Maxwellian during the power on pulse. When the plasma power is turned off, inelastic collisions and diffusion cooling result in a fast decay of T_e , first in the tail of the EEPF, where inelastic collisions dominate, and later in the bulk. The EEPF microseconds after terminating power is a bi-Maxwellian, with the temperature of the bulk relatively

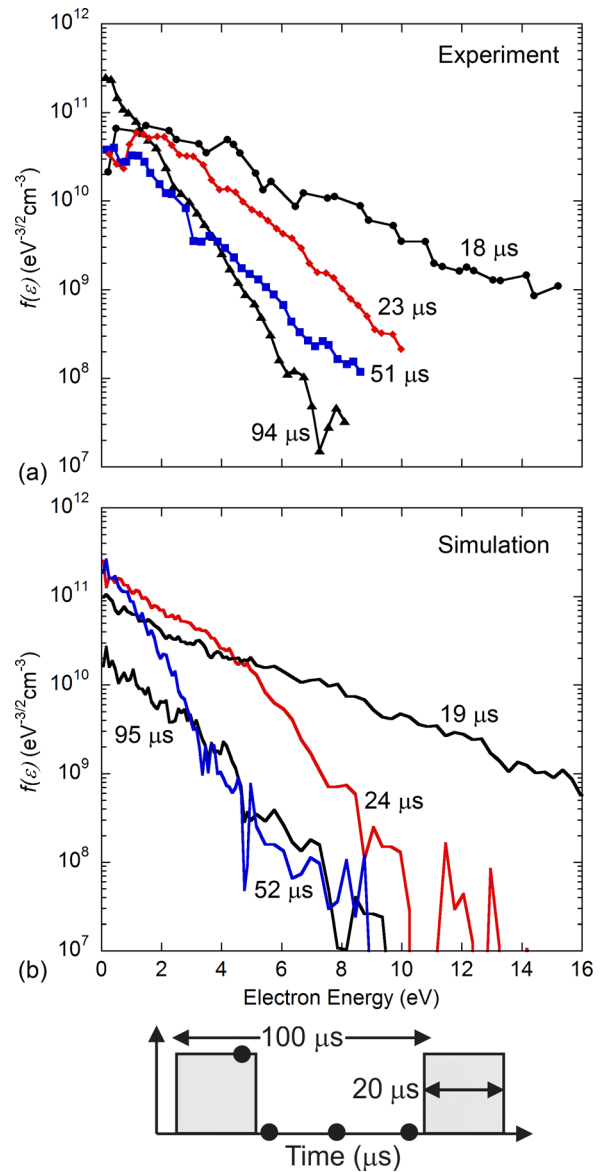


FIG. 5. Time-resolved electron energy probability functions (EPPFs) when the pulsed main plasma and the auxiliary plasma are both on, obtained from the (a) experiments and (b) simulations. The times of the EPPFs relative to the start of the 20 μs power pulse are shown in the lower schematic.

unchanged from the power on period due to its low rate of power loss, while the temperature of the tail rapidly decreases. After about 10 μs into the afterglow, T_e is too low for electrons to undergo significant inelastic collisions in argon. At this point, elastic thermalization collisions and diffusion cooling are the dominant cooling mechanisms. The EEPFs at this point appear Maxwellian as the plasma density is still high enough for electron-electron collisions to thermalize the distribution. On the timescale of the inter-pulse period, the asymptotic value of $T_e = 0.7 \text{ eV}$ is sustained by superelastic heating by quenching of long-lived metastable excited states of argon. For example, from calculations of the electron energy distribution by solving Boltzmann's equation, for $T_e \approx 0.7 \text{ eV}$, the thermalization (cooling) rate is about 25 eV/s. This cooling rate can be balanced by superelastic heating for an excited state density of 10^{10} cm^{-3} , which is commensurate with what is expected (and

computed) for these conditions. The predictions for T_e from the simulations, shown in Fig. 3(c), accurately capture the experimental trends.

When the auxiliary (upper) plasma is on, there is the possibility to exchange electrons between the two plasma sources. Due to the confining plasma potential of each individual plasma source, the electrons that escape from one source and transport to the other source (auxiliary-to-main or main-to-auxiliary) are from the tail of the EEPF. Only the more energetic electrons are able to scale the plasma potential barrier at the boundary of one plasma source to transfer to the other plasma source. If the boundary regions on either side of the grid are not collisional, then the electron that loses energy scaling the potential hill from one source gains back energy being accelerated into the volume of the adjacent source by its plasma potential. This flux of electrons originating from the adjacent plasma source is termed the *external heating flux*. The absolute value of the external flux is small since this flux originates in the tail of the EEPF.

The plasma potential near the axis (passing through the center of the open portion of the grid) as computed by the model is shown in Fig. 6 for the auxiliary plasma being on and off. There is no active control of the plasma potential in either of the sources. Values are shown at the end of the active-glow power pulse and at the end of the afterglow. During the active-glow of the pulse, the plasma potential is predicted to be 3–4 V higher in the auxiliary plasma. This difference is likely larger in reality as the measured value of T_e (≈ 3.5 eV) in the main plasma is lower than that in the auxiliary plasma ($T_e \approx 4.5$ eV) by 1 eV. High energy electrons that overcome the potential barrier in the auxiliary plasma and, passing through the grid, are accelerated into the main plasma. Energetic electrons also overcome the potential barrier of the main plasma and are accelerated into the auxiliary plasma. The higher plasma potential of the upper plasma compared to the lower plasma leads to a net loss of high energy electrons from the lower main plasma to the upper auxiliary plasma. (Note that the minimum in plasma potential between the grids presents a relatively low barrier

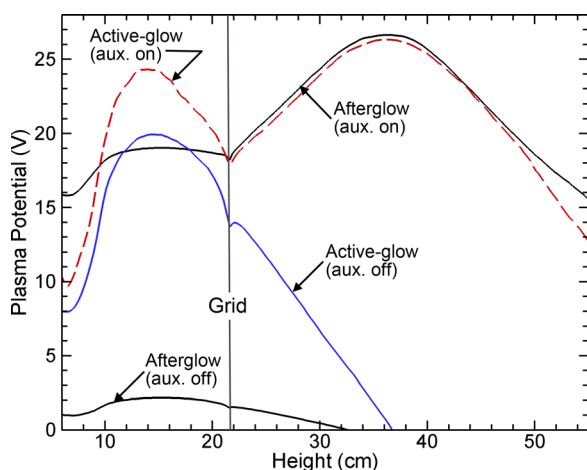


FIG. 6. Plasma potentials along the axis passing through the central opening of the grid predicted by the model at the end of the active-glow and the end of the afterglow. Values are shown with and without the cw auxiliary plasma.

compared to the plasma potential barrier in the absence of the adjacent plasma.) Although the absolute flux of these electrons is small, they are from the tail of the distribution function, which would otherwise be reflected by the plasma potential hill and return to produce ionization. The end result is a decrease in n_e in the main plasma when both plasmas are on, as shown in Fig. 3, due to the lower potential barrier. Positive ions are injected from the auxiliary plasma to the main plasma. In the opposite direction, however, positive ions from the main plasma accelerate in the region below the grid but cannot overcome the larger potential barrier of the upper plasma in the region above the grid.

Since T_e of the upper plasma is higher than that of the lower plasma during the afterglow, there is a net injection of high energy electrons from the auxiliary plasma to the main plasma—the *external heating flux*. When both plasmas are on, the magnitude of the external heating flux entering the main plasma is small compared to the heating by its own inductively coupled electric fields. As a result, there is only a nominal effect on the shapes of the EEPFs. Experimentally and computationally, the shapes of the EEPFs in the main (lower) plasma source when its power is on depend little on whether the auxiliary (top) plasma source is on or off. However, during the afterglow of the pulsed main plasma when the far more dominating ICP heating source is off, superelastic collisions and the external heating flux are the main source of electron heating. The magnitude of the external heating flux remains relatively constant, while the electron density and superelastic heating source in the main plasma source decrease. By 60–70 μ s (40–50 μ s into the afterglow), the external heating flux produces a net increase in the T_e of the main plasma, reaching 1.7 eV at the end of the afterglow. The computed values of T_e , shown in Fig. 3, also reflect the contributions of the external heating flux.

The consequences of the external heating flux from the auxiliary plasma on the main plasma during the afterglow are clearly evident in the EEPFs, shown in Fig. 5, compared to the EEPFs without the auxiliary plasma, shown in Fig. 4. Note that the computed EEPFs result from collecting pseudo-particles in slices of 1/200th of the pulsed period averaged over a volume at the location of the probe of about 0.5 cm in radius and height. This time and spatial resolution introduces some noise. The EEPFs during the active-glow while the main plasma power is on have the same characteristic shape regardless of whether the auxiliary plasma is on or off. However, during the afterglow when the auxiliary plasma is on, the tails of the EEPFs of the main plasma are elevated, extending to energies of 8–10 eV. In the absence of the auxiliary plasma, the tails of the EEPFs late in the afterglow extend to only 2–4 eV. The computed EEPFs show these same trends.

Additional insights to these processes come from the simulated plasma properties shown in Fig. 2. The electron density and electron impact ionization source, S_e , are shown at the end of the active-glow and end of the afterglow when the auxiliary source is on. The S_e is a measure of the presence of high energy electrons and so is largest in the skin depth of the electromagnetic field at the radial periphery of the plasma. At the end of the active-glow, the extent of the

electron density is still rising in both sources and diffusing towards each other. The S_e is nearly mirrored across the grid as electrons from both sources cross over to the other source. At the end of the afterglow of the main plasma, the ionization source in the auxiliary plasma changes little. However, at this time, significant S_e in the main plasma results only from electrons injected from the upper auxiliary plasma. The ionization from these sparse injected electrons appears as the tracks of S_e leading from the upper into the lower plasma. (The sharp bends in the tracks result from individual simulation particles undergoing a velocity deflecting collision.) Although these energetic electrons from the auxiliary plasma are sparse, they are nevertheless sufficient to provide net heating to the tail of the EEPF in the main plasma. This heating raises the plasma potential significantly above that in the absence of the auxiliary plasma.

The ability to affect the EEPF in the main plasma by the auxiliary source relies, in part, on the contributions of high energy electrons that have sufficient mean free path to penetrate into the main plasma. As such, this control depends on pressure. Increasing pressure reduces the energy relaxation length and so leads to more isolation between the plasma sources. From computational results, based on values at the middle of the main plasma, we expect that the plasmas will appear to operate independently at pressures exceeding about 25 mTorr.

IV. CONCLUDING REMARKS

A plasma reactor incorporating dual tandem ICP sources (main and auxiliary source), separated by a grounded grid, was used to manipulate the EEPF in the afterglow of the main pulsed plasma. By operating the auxiliary source on a cw basis, T_e during the afterglow of the main plasma source could be increased to a value (1.7 eV) above that of the afterglow plasma alone (0.7 eV) but below that of a continuous plasma (3.5 eV). Hot electron transport from the auxiliary plasma to the main plasma provided background heating that sustained the tail of the EEPF during the afterglow of the pulsed main ICP. As n_e decreased during the afterglow, a continuous influx of hot electrons produced an increase in T_e in the main plasma. This is a demonstration of *external control* of the EEPF. Simulations captured the experimentally measured trends in the EEPF and T_e and demonstrated the

importance of the *small external heating flux* in determining the properties of the main plasma.

ACKNOWLEDGMENTS

This work was supported by the Department of Energy, Office of Fusion Energy Science, Contract No. DE-SC0001939, the National Science Foundation Grant Nos. CBET 0903426 and CDI-1124724, and the Semiconductor Research Corp.

- ¹V. M. Donnelly and A. Kornblit, *J. Vac. Sci. Technol. A* **31**, 050825 (2013).
- ²T. Makabe and Z. Lj. Petrovic, *Plasma Electronics: Applications in Microelectronic Device Fabrication*, 2nd ed. (CRC Press, 2014).
- ³H. Sugai, I. Ghanashev, M. Hosokawa, K. Mizuno, K. Nakamura, H. Toyoda, and K. Yamauchi, *Plasma Sources Sci. Technol.* **10**, 378 (2001).
- ⁴V. A. Godyak, *Phys. Plasmas* **20**, 101611 (2013).
- ⁵S. Samukawa, Y. Nakagawa, T. Tsukada, H. Ueyama, and K. Shinohara, *Appl. Phys. Lett.* **67**, 1414 (1995).
- ⁶H. Shin, W. Zhu, D. J. Economou, and V. M. Donnelly, *J. Vac. Sci. Technol. A* **30**, 031304 (2012).
- ⁷G. A. Heibner and C. B. Fleddermann, *J. Appl. Phys.* **82**, 2814 (1997).
- ⁸A. Maresca, K. Orlov, and U. Kortshagen, *Phys. Rev. E* **65**, 056405 (2002).
- ⁹M.-H. Lee, J.-H. Ku, K.-T. Hwang, and C.-W. Chung, *Phys. Plasmas* **16**, 063506 (2009).
- ¹⁰K. Kato, S. Iizuka, and N. Sato, *Appl. Phys. Lett.* **65**, 816 (1994).
- ¹¹K. Kato, T. Shimizu, S. Iizuka, and S. Sato, *Appl. Phys. Lett.* **76**, 547 (2000).
- ¹²J. I. Hong, S. H. Seo, S. S. Kim, N. S. Yoon, C. S. Chang, and H. Y. Chang, *Phys. Plasmas* **6**, 1017 (1999).
- ¹³A. Aanesland, J. Bredin, P. Chabert, and V. Godyak, *Appl. Phys. Lett.* **100**, 044102 (2012).
- ¹⁴S. Uhm, L.-H. Lee, H. Y. Chang, and C. W. Chung, *Phys. Plasmas* **11**, 4830 (2004).
- ¹⁵H. Shin, W. Zhu, L. Xu, V. M. Donnelly, and D. J. Economou, *Plasma Sources Sci. Technol.* **20**, 055001 (2011).
- ¹⁶H. Shin, W. Zhu, D. J. Economou, and V. M. Donnelly, *J. Vac. Sci. Technol. A* **30**, 031304 (2012).
- ¹⁷C.-K. Kim and D. J. Economou, *J. Appl. Phys.* **91**, 2594 (2002).
- ¹⁸M. J. Kushner, *J. Phys. D: Appl. Phys.* **42**, 194013 (2009).
- ¹⁹M. D. Logue, H. Shin, W. Zhu, L. Xu, V. M. Donnelly, D. J. Economou, and M. J. Kushner, *Plasma Sources Sci. Technol.* **21**, 065009 (2012).
- ²⁰S.-H. Song and M. J. Kushner, *Plasma Sources Sci. Technol.* **21**, 055028 (2012).
- ²¹P. Tian and M. J. Kushner, *Plasma Sources Sci. Technol.* **24**, 034017 (2015).
- ²²M. V. Malyshev, V. M. Donnelly, J. I. Colonell, and S. Samukawa, *J. Appl. Phys.* **86**, 4813 (1999).
- ²³M. V. Malyshev and V. M. Donnelly, *Plasma Sources Sci. Technol.* **9**, 353 (2000).
- ²⁴B. Ramamurthi and D. J. Economou, *Plasma Sources Sci. Technol.* **11**, 324 (2002).